forms of the membrane-bound receptors that can bind ligand in a way similar to that of their membrane-bound counterparts. As a result, these receptors play an important role in the regulation of normal receptor activity and autoimmune disease (*11*). Elevated serum concentrations of a soluble Fas were found in over one-half of patients with SLE, and soluble Fas is capable of inhibiting Fas-mediated apoptosis in vitro and altering lymphocyte development and proliferation in response to self antigen in vivo. These findings suggest a critical role for this molecule in autoimmune diseases. Therapies such as plasmapheresis that may remove soluble Fas from sera of SLE patients may restore normal apoptosis and reduce autoimmune disease (*12*). Also, in light of the fact that Fas-mediated apoptosis has been implicated in lymphocyte apoptosis in HIV infection (*3*), it is of great importance to investigate a role for FasΔTM in immunodeficiencies and whether blockade of Fas-mediated apoptosis in vivo, with the use of recombinant FasΔTM molecules, is of clinical use in such disease conditions.

REFERENCES AND NOTES

1. N. Itoh *et al.*, *Cell* **66**, 233 (1991); R. Watanabe-Fukunaga *et al.*, *J. Immunol.* **148**, 1274 (1992); A. Oehm *et al.*, *J. Biol. Chem.* **267**, 10709 (1992); N. Itoh and S. Nagata, *ibid.* **268**, 10932 (1993).
2. R. Watanabe-Fukunaga, C. I. Brannan, N. G. Copeland, N. A. Jenins, S. Nagata, *Nature* **356**, 314 (1992); M. L. Watson *et al.*, *J. Exp. Med.* **176**, 1645 (1992); M. Adachi, R. Watanabe-Fukunaga, S. Nagata, *Proc. Natl. Acad. Sci. U.S.A.* **90**, 1756 (1993); J. Wu, T. Zhou, J. He, J. D. Mountz, *J. Exp. Med.* **178**, 461 (1993).
3. J. F. Krowka, B. Cuevas, M. S. Ascher, H. W. Sheppard, unpublished data.
4. L. B. Owen-Schaub, S. Yonehara, W. L. Crump III, E. A. Grimm, *Cell. Immunol.* **140**, 197 (1992).
5. Y. Gavrieli, Y. Sherman, S. A. Ben-Sasson, *J. Cell Biol.* **119**, 493 (1992).
6. S. Takashi, T. Takahashi, P. Golstein, S. Nagata, *Cell* **75**, 1169 (1993).
7. O. Josimovic-Alasevic, T. Herrmann, T. Diamantstein, *Eur. J. Immunol.* **18**, 855 (1988).
8. T. J. Schall *et al.*, *Cell* **61**, 361 (1990).
9. B. Mosley *et al.*, *ibid.* **59**, 335 (1989).
10. R. G. Goodwin *et al.*, *ibid.* **60**, 941 (1990).
11. R. Fernandez-Botran, *FASEB J.* **5**, 2567 (1991).
12. D. J. Wallace, *N. Engl. J. Med.* **327**, 1029 (1992).
13. D. M. Klinman *et al.*, *J. Exp. Med.* **163**, 1292 (1986).
14. E. M. Tan *et al.*, *Arthritis Rheum.* **25**, 1277 (1982).
15. G. Frizzera, Y. Kaneko, M. Sakurai, *J. Leukemia* **3**, 1 (1989); A. Ohsaka *et al.*, *J. Cancer* **69**, 1259 (1992).
16. RNA (10 μg) isolated with the use of the guanidine isothiocyanate–acid phenol method was used for first-strand cDNA syntheses. Two oligonucleotides, 5′-CACTTCGGAGGATTGCTCAACA-3′ (nt 170 to 191) and 5′-TATGTTGGCTCTTCAGC GCTA-3′ (complementary to nt 1316 to 1336), were used to amplify human Fas mRNA by PCR. The PCR products were analyzed and recovered from agarose gels and subcloned into a pCR vector (Invitrogen, San Diego, CA).
17. For genomic PCR, primers were designed to flank each of the putative introns. Human genomic DNA (0.5 μg) was used as a template in each PCR reaction. All nucleotide sequences were determined by the dideoxy chain termination method with the use of modified bacteriophage T7 DNA polymerase (United States Biochemical).
18. The full-length Fas and the FasΔTM cDNAs were inserted into the Eco RI cloning site of pcDNA I (Invitrogen). The orientations of the insert were determined with Hind III digestion. COS-7 cells were transfected with the use of DEAE-dextran. After 72 hours, single cell suspensions were stained with the mouse monoclonal antibody to human Fas [immunoglobulin M (IgM)] (Upstate Biotechnology, Lake Placid, NY). After washing, the cells were stained with fluorescein isothiocyanate (FITC)–conjugated goat IgM to mouse (Southern Biotechnology, Birmingham, AL) for 30 min. As a control, the same cells were similarly treated, except that the primary antibody was replaced with an unrelated mouse IgM.
19. Cells were stimulated with PHA-P (10 μg/ml) (Pharmacia, Piscataway, NJ) for 48 hours. Approximately 5×10^5 stimulated cells were then cultured in a flat-bottom 96-well plate in RPMI 1640–10% fetal calf serum and IgM (200 ng/ml) in the presence of serial dilutions of supernatants derived from the COS-7 cells that were transfected with either Fas cDNA or FasΔTM expression plasmids and cultured for 3 days. After 12 hours of incubation, 2×10^5 cells were cytospun onto poly-L-lysine–pretreated slides, fixed in 10% (v/v) formalin at room temperature for 12 hours, and stained for in situ apoptosis. A minimum of 200 lymphocytes were counted in 10 randomly selected microscopic fields by an observer unaware of the cell culture condition. The apoptosis analysis of CEM-6 cells was carried out in a similar manner.
20. Sera were first diluted to a ratio of 1:5 in borate-buffered saline (BBS), and Ig complexes were absorbed with anti-human Ig beads at 4°C for 12 hours. Plates were precoated with IgM (2 μg/ml). After blocking, the absorbed sera were added and incubated for 4 hours at room temperature. After extensive washing, the bound antibody was detected with an antibody to mouse IgG1 that is isotype-specific and reports alkaline phosphatase, and the plates were incubated with *p*-nitrophenylphosphate substrate.
21. A 530-bp extracellular Fas sequence (nt 26 to 556) (*1*) was PCR-amplified from a mouse *fas* cDNA clone and ligated into a pSP65 vector that contained the hinge, CH2 and CH3 sequence of human IgG1 (hIgG1) [R. G. Goodwin *et al.*, *Cell* **73**, 447 (1993)]. The fusion gene was sequenced to confirm that the *fas* extracellular domain was in frame with the hIgG1 fragment. The *fas-hIgG1* fusion gene was transfected into COS cells and transiently expressed as a secreted fusion protein. This protein was purified with an anti-hIgG1 agarose affinity column and could bind to the Fas ligand (*5*).
22. MTT (Sigma) was dissolved in BBS to make a solution (5 mg/ml). The MTT-BBS solution (10 μl) was added to each well (containing 100 μl of cells) and incubated for 4 hours at 37°C in a 5% CO_2 humidified incubator. 100 μl of 0.04 M HCl in isopropanol was added to each well and was vigorously mixed by pipeting. The plates were read in a microtiter plate reader (Emax, Molecular Division, Menlo Park, CA), with the use of a 570-nm filter. Background noise was subtracted with a dual-wavelength setting of 650 nm.

23. We thank W. J. Koopman for helpful discussions, V. Prochazka for genomic DNA sequencing, T. F. Tedder for providing the hIgG1-pSP65 plasmid, J. F. Krowka for communicating results before publication, and B. K. Bunn for expert secretarial assistance in typing the manuscript. Supported in part by a Veterans Administration (VA) Merit Review Award; a VA Career Development Award; and grants P60 AR20614, P50 AI23694, P01 AR03555, and R01 AI30744 from the National Institutes of Health.

19 November 1993; accepted 4 February 1994

High-Resolution Solution Structure of the β Chemokine hMIP-1β by Multidimensional NMR

Patricia J. Lodi, Daniel S. Garrett, John Kuszewski, Monica L.-S. Tsang, James A. Weatherbee, Warren J. Leonard, Angela M. Gronenborn,* G. Marius Clore*

The three-dimensional structure of a member of the β subfamily of chemokines, human macrophage inflammatory protein–1β (hMIP-1β), has been determined with the use of solution multidimensional heteronuclear magnetic resonance spectroscopy. Human MIP-1β is a symmetric homodimer with a relative molecular mass of ~16 kilodaltons. The structure of the hMIP-1β monomer is similar to that of the related α chemokine interleukin-8 (IL-8). However, the quaternary structures of the two proteins are entirely distinct, and the dimer interface is formed by a completely different set of residues. Whereas the IL-8 dimer is globular, the hMIP-1β dimer is elongated and cylindrical. This provides a rational explanation for the absence of cross-binding and reactivity between the α and β chemokine subfamilies. Calculation of the solvation free energies of dimerization suggests that the formation and stabilization of the two different types of dimers arise from the burial of hydrophobic residues.

Human macrophage inflammatory protein–1β, also known as Act-2, is a member of the β chemokine (chemotactic cytokine) subfamily of proteins (*1*, *2*). These proteins, as well as the related α chemokines, comprise a polypeptide chain of ~8 to 10 kD and contain four cysteine residues at near-identical positions. The distinction between the α and β chemokine subfamilies was initially based on whether the first two cysteine residues are separated by one residue (α) or are adjacent (β). This division also extends to chromosomal location (chromosomes 4 and 17 for the α and β chemokines, respectively) and function. Thus, whereas the α chemokines (for example, IL-8) are potent chemoattractants

and activators of neutrophils but not monocytes, the β chemokines exhibit chemoattractant potential for monocytes and lymphocytes but not for neutrophils (*2, 3*). Members within each subfamily exhibit 25 to 70% sequence identity, whereas the amino acid identity between members of the two subfamilies ranges from 20 to 40% (*2, 3*). Here, we present the determination of the three-dimensional structure of hMIP-1β in solution using heteronuclear magnetic resonance (NMR) spectroscopy.

As hMIP-1β aggregates at pH values above 3.5, all NMR experiments were carried under conditions (pH 2.5) where hMIP-1β exists as a discrete and stable dimer with a molecular mass of 15.6 kD (*4*). Because of the complexity of the system, the structure determination was carried out on uniformly isotopically labeled protein (*5*) and involved the application of double and triple resonance NMR spectroscopy (*6*). The structural statistics for the final ensemble of 35 simulated annealing structures (*7–9*) are summarized in Tables 1 and 2, and stereo views of best-fit superpositions, illustrating both the backbone for the complete dimer and ordered side chains for a single subunit, are shown in Fig. 1. With the exception of residues 1 to 3, which are partially disordered, the structure is exceptionally well defined both at the monomer and dimer levels (Table 2).

Within each subunit, the main secondary structure elements comprise a triple-stranded antiparallel β sheet (residues 26 to 31, 39 to 44, and 48 to 52) arranged in a Greek key, on top of which lies an α helix (residues 57 to 68) (Figs. 1B and 2A). The NH_2-terminus comprises an irregular strand and a series of nonclassical turns that form a long loop extending from residues 12 to 20. This is followed by a four-residue helical turn (residues 21 to 24), which leads into strand β1. The two disulfide bridges have a left-handed spiral conformation. There are two tightly bound water molecules that serve to bridge hydrogen bonds: one between the backbone amide of Cys^{12} and the backbone carbonyls of Gln^{37} and Pro^{38}, thereby orienting the NH_2-terminus with regard to strand β2, and the second between the backbone amide of Gln^{37} and the backbone carbonyl and side chain Sγ atom of Cys^{35}, thereby stabilizing the loop between strands β1 and β2. The positioning of the helix with regard to the underlying β sheet is determined by numerous hydrophobic interactions (Fig. 1B). In addition to the regular backbone hydrogen bonding within the secondary structure elements, there are three hydrogen bonding interactions involving side chains that are of interest: namely, between the Oγ of Thr^{31} and the backbone amide of Ala^{39}, between the Oγ(H) atoms of Thr^{44} and Ser^{47}; and between the aromatic ring of Tyr^{15} and the carboxylate of Asp^{53}.

The structure of the hMIP-1β monomer is very similar to that of IL-8 (*10, 11*). The Cα atoms of 59 residues can be superimposed with a root-mean-square (rms) difference of 1.6 Å (Fig. 2). The sequence identity within this region is 20%. Buried residues that are important for maintaining the structure of the monomer are either the same or substituted

Table 1. Structural statistics. The notation of the NMR structures is as follows: SA are the final 35 simulated annealing structures; $\overline{SA}$ is the mean structure obtained by averaging the coordinates of the individual SA structures best-fitted to each other (excluding residues 1 to 3 of both subunits); and $(\overline{SA})r$ is the restrained minimized mean structure obtained by restrained regularization of the mean structure $\overline{SA}$. The number of terms for the various restraints is given in parentheses and applies to the entire dimer.

Structural statistics	<SA>	$(\overline{SA})r$
Rms deviations from experimental distance restraints (Å)*		
All (3264)	0.026 ± 0.001	0.030
Intrasubunit		
Interresidue sequential ($\|i - j\| = 1$) (670)	0.034 ± 0.001	0.039
Interresidue short range ($1 < \|i - j\| \leq 5$) (462)	0.025 ± 0.002	0.032
Interresidue long range ($\|i - j\| > 5$) (860)	0.026 ± 0.002	0.031
Intraresidue (908)*	0.019 ± 0.002	0.021
Bound water (28)†‡	0.023 ± 0.003	0.025
H bond (92)‡	0.040 ± 0.012	0.037
Intersubunit		
Interproton (228)	0.024 ± 0.005	0.018
H bond (16)‡	0.046 ± 0.015	0.043
Rms deviation from the cross-validated experimental distance test sets (Å)§	0.074 ± 0.02	
Rms deviations from $^3J_{HN\alpha}$ coupling constants (Hz) (102)*	0.54 ± 0.02	0.52
Rms deviations from experimental dihedral restraints (degrees) (220)*	0.55 ± 0.03	0.47
Deviations from idealized covalent geometry‖		
Bonds (Å) (2170)	0.005 ± 0.000	0.005
Angles (degrees) (3900)	0.739 ± 0.009	0.774
Impropers (degrees) (1150)	0.418 ± 0.036	0.478
E_{L-J} (kcal mol^{-1})¶	−592 ± 16	−572

*None of the structures exhibits distance violations greater than 0.3 Å, dihedral angle violations greater than 5°, or $^3J_{HN\alpha}$ coupling constant violations greater than 2 Hz. Furthermore, there are no systematic interproton distance violations between 0.1 and 0.3 Å among the ensemble of calculated structures, and the average number of $^3J_{HN\alpha}$ coupling constant violations between 1 and 2 Hz is 5.5 ± 1.8. In addition, all the φ,ψ backbone torsion angles lie within the allowed regions of the Ramachandran plot. The $^3J_{HN\alpha}$ coupling constants included directly in the refinement comprised only those that could be measured from the 3D HNHA experiment to an accuracy of 0.5 Hz or better. Thus, couplings associated with resonances that exhibit overlap of their ^{15}N and NH chemical shifts were not included. The torsion angle restraints comprise 122 φ, 10 ψ, 80 χ_1, and 8 χ_2 angles with minimum ranges of ±10°, ±50°, ±20°, and ±20°, respectively. The narrow range for some of the φ restraints was made possible by the availability of highly accurate $^3J_{HN\alpha}$ coupling constant data. In all cases the angular standard deviations of the torsion angles for the ensemble of 35 SA structures were much smaller than the ranges used for the corresponding torsion angle restraints. Only structurally useful intraresidue NOEs are included in the interproton distance restraints. Thus, NOEs between protons separated by two bonds or between nonstereospecifically assigned protons separated by three bonds are not incorporated in the restraints. The values of the interproton distance, torsion angle, and $^3J_{HN\alpha}$ restraints energy terms are 67.8 ± 4.2, 4.03 ± 0.5, and 29.7 ± 2.0 kcal mol^{-1}, respectively, using force constants of 30 kcal mol^{-1} Å^{-2}, 200 kcal mol^{-1} rad^{-2}, and 1 kcal mol^{-1} Hz^{-2}, respectively. †The distance restraints involving the four bound water molecules (two per subunit) comprise four interproton distance restraints between backbone amide protons and water protons and 24 distance restraints relating to hydrogen bonds. The latter comprise the water-bridging hydrogen bonds from Cys^{12}(NH) to Gln^{37}(O) and Pro^{38}(O), and from Ser^{36}(NH) to Cys^{35}(Sγ) and Cys^{35}(O). ‡For each backbone hydrogen bond there are two distance restraints: r_{NH-O} (1.7 to 2.5 Å) and r_{N-O} (2.3 to 3.5 Å). These hydrogen bonding restraints account for the slowly exchanging amide protons and were included only in the final stages of refinement. §Simulated annealing with complete cross-validation (*24*) was carried out on the final set of 35 SA structures. For each simulated annealing run with cross-validation, the data set was randomly partitioned into a test set comprising ~10% of the data and a reference set. Only the latter is included in the target function that is minimized. The test set for each SA structure was therefore different, and the value of the average rms deviation for all the test sets is quoted. The average number of distance violations greater than 0.5 Å in the test sets was 1.3 ± 0.9. The low average values of the rms deviations and violations for the test sets indicate the high degree to which each distance can be predicted by the remaining ones. The atomic rms distribution about the mean coordinate positions remains essentially unchanged upon complete cross-validation, and there is no significant shift in the atomic coordinates—that is, the difference between the mean coordinate positions before and after complete cross-validation is smaller than the rms distribution of the individual structures about their mean coordinate positions. These results indicate the high degree of completeness of the experimental data and provide a reliable indication of the high accuracy of the structures (*24*). ‖The improper torsion restraints serve to maintain planarity and chirality. ¶E_{L-J} is the Lennard-Jones van der Waals energy calculated with the CHARMM (*25*) empirical energy function and is not included in the target function for simulated annealing or restrained minimization.

P. J. Lodi, D. S. Garrett, J. Kuszewski, A. M. Gronenborn, G. M. Clore, Laboratory of Chemical Physics, National Institute of Diabetes and Digestive and Kidney Diseases, National Institutes of Health, Bethesda, MD 20892, USA.
M. L.-S. Tsang and J. A. Weatherbee, R&D Systems, Minneapolis, MN 55413, USA.
W. J. Leonard, Section on Pulmonary and Molecular Immunology, National Heart, Lung and Blood Institute, National Institutes of Health, Bethesda, MD 20892, USA.
*To whom correspondence should be addressed.

Table 2. Atomic rms differences. The notation of the structures is the same as that in Table 1. In addition to the low atomic rms differences, the angular rms deviations for the backbone ϕ and ψ torsion angles of residues 4 to 69, and for the χ_1 angles of the 47 residues per subunit that do not exhibit rotamer averaging, are also very low, with values of 1.4 ± 2.0°, 2.4 ± 2.9°, and 2.0 ± 2.4°, respectively. This high degree of precision is expected, given the large number of experimental NMR restraints—namely, an average of 26 per residue (*26*). The restrained minimized mean structure for the monomer, which would be obtained by restrained regularization of the mean monomer structure calculated by averaging the coordinates of the 35 SA structures best-fitted to only a single subunit, was not computed (blank spaces).

Comparison	Atomic rms differences (excluding residues 1 to 3) (Å)					
	Dimer			Monomer		
	Backbone atoms	All atoms	All ordered atoms*	Backbone atoms	All atoms	All ordered atoms*
<SA> versus $\overline{SA}$	0.30 ± 0.09	0.71 ± 0.08	0.45 ± 0.09	0.20 ± 0.05	0.65 ± 0.06	0.38 ± 0.06
<$\overline{SA}$> versus $(\overline{SA})r$	0.33 ± 0.12	0.79 ± 0.09	0.49 ± 0.10			
$(\overline{SA})r$ versus SA	0.10	0.38	0.19			

*The atoms included comprise all N, Cα, C, O, and Cβ atoms of residues 4 to 69, the complete side chains of residues Pro^7, Pro^8, Thr^9, Cys^{11}, Cys^{12}, Phe^{13}, Ser^{14}, Tyr^{15}, Thr^{16}, Leu^{20}, Pro^{21}, Phe^{24}, Val^{25}, Val^{26}, Tyr^{28}, Tyr^{29}, Thr^{31}, Ser^{33}, Leu^{34}, Cys^{35}, Val^{40}, Val^{41}, Phe^{42}, Thr^{44}, Val^{50}, Cys^{51}, Trp^{58}, Val^{59}, Tyr^{62}, Val^{63}, Tyr^{64}, Leu^{66}, Leu^{68}, and the side chains of Arg^{18} up to Cδ, Lys^{19} up to Cε, Arg^{22} up to Cγ, Asp^{27} up to Cγ, Glu^{30} up to Cδ, Gln^{37} up to Cγ, Gln^{43} up to Cγ, Lys^{45} up to Cε, Arg^{46} up to Cδ, Glu^{56} up to Cδ, Glu^{61} up to Cδ, Aps^{65} up to Cγ, and Glu^{67} up to Cδ.

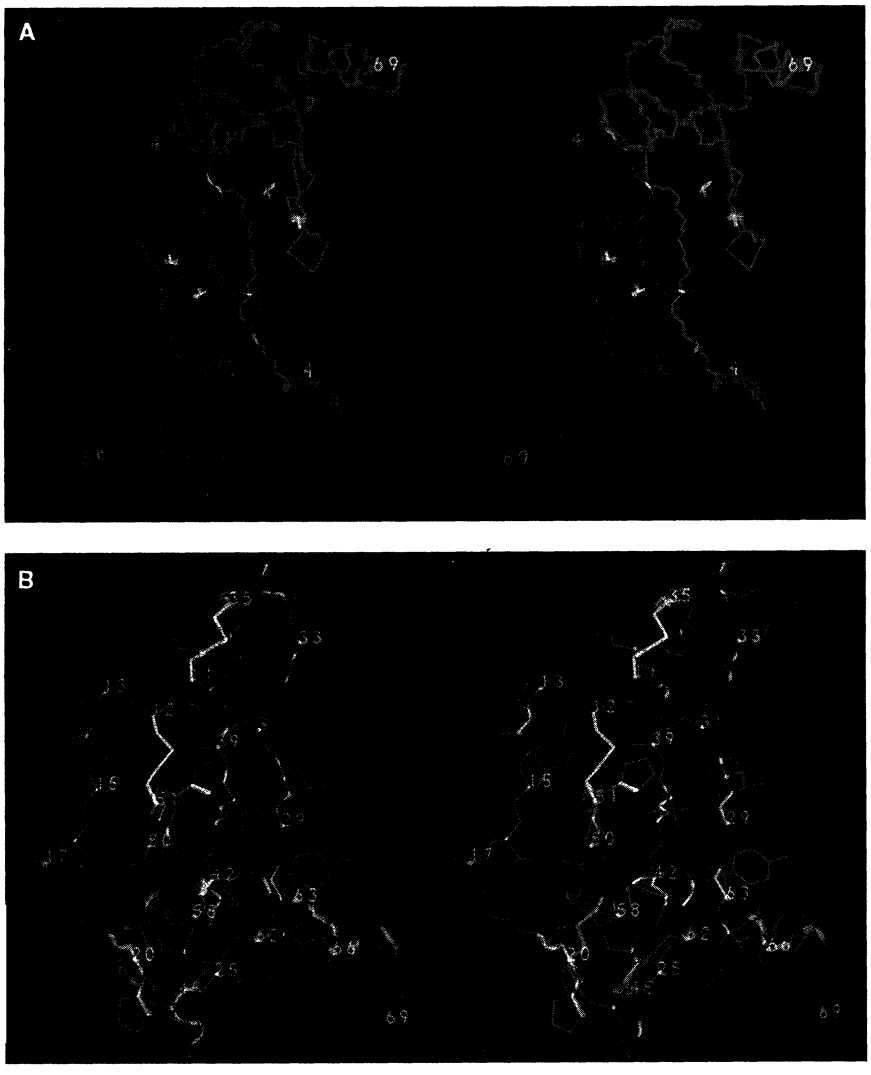

Fig. 1. Stereo views showing best-fit superpositions of the (**A**) backbone atoms and (**B**) ordered side chains of the 35 simulated annealing structures of hMIP-1β. The hMIP-1β dimer is shown in (A) with one subunit in blue, the other in red, and the tightly bound water molecules in yellow; a single subunit of hMIP-1β is displayed in (B) with the backbone in blue, the side chains in red, the disulfide bridges in yellow, and the bound water molecules in green. The numbers indicate residue numbers along the sequence and are located close to the Cα positions.

conservatively. Surface residues necessary for dimer formation and receptor binding, however, vary substantially between the two subfamilies of chemokines.

There are four significant structural differences between hMIP-1β and IL-8 at the monomer level. First, the conformation of the first disulfide bridge is a right-handed hook in IL-8 as opposed to a left-handed spiral in hMIP-1β. This is associated with the insertion in IL-8 of a residue between the first two cysteines and of two residues in the turn connecting β strands 1 and 2 (Fig. 2B). Second, the helix extends five residues further at the COOH-terminus in IL-8 compared to hMIP-1β. Third, the conformation of the turn connecting strands β2 and β3 differs around residues 46 and 47. Finally, the direction of the NH_2-terminal residues preceding the first cysteine is completely different. The latter three differences at the monomer level are related to the different quaternary structures of the two proteins.

The quaternary structures of hMIP-1β and IL-8 are completely different (Fig. 3). When one subunit of hMIP-1β is superimposed on one subunit of IL-8, the Cα atomic rms displacement between the second subunit of hMIP-1β and the second subunit of IL-8 is 34 Å (Fig. 3D). Different quaternary structures for essentially identical monomer units are clearly very rare occurrences and to our knowledge have been observed in cases with significant sequence identity (that is, greater than 15 to 20%) on only two previous occasions (*12*).

The IL-8 dimer is globular in shape with dimensions of 40 by 42 by 32 Å (Fig. 3C), whereas the hMIP-1β dimer is elongated and cylindrical with dimensions of 56 by 30 by 26 Å (Fig. 3, A and B). In the case of IL-8, the C_2 axis is located between the CαH protons of Arg^{26} and $Arg^{26'}$ in the middle of strand β1 (equivalent to residue 29 of hMIP-1β). This results in a structure with a six-stranded anti-

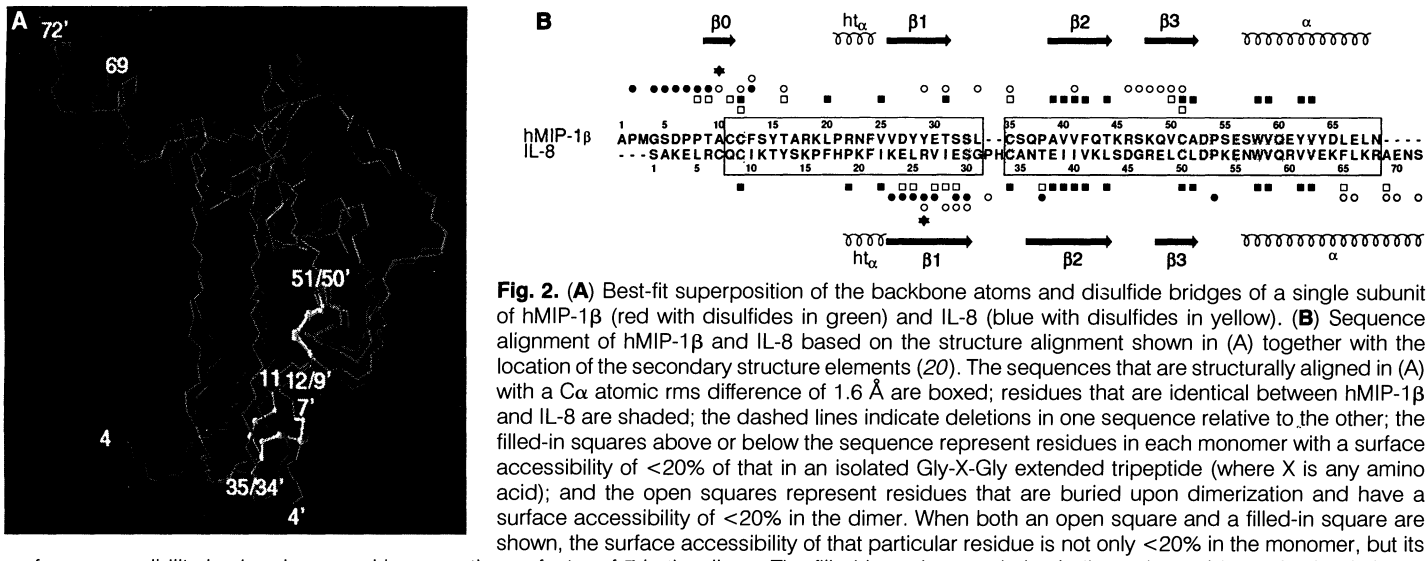

Fig. 2. (**A**) Best-fit superposition of the backbone atoms and disulfide bridges of a single subunit of hMIP-1β (red with disulfides in green) and IL-8 (blue with disulfides in yellow). (**B**) Sequence alignment of hMIP-1β and IL-8 based on the structure alignment shown in (A) together with the location of the secondary structure elements (*20*). The sequences that are structurally aligned in (A) with a Cα atomic rms difference of 1.6 Å are boxed; residues that are identical between hMIP-1β and IL-8 are shaded; the dashed lines indicate deletions in one sequence relative to the other; the filled-in squares above or below the sequence represent residues in each monomer with a surface accessibility of <20% of that in an isolated Gly-X-Gly extended tripeptide (where X is any amino acid); and the open squares represent residues that are buried upon dimerization and have a surface accessibility of <20% in the dimer. When both an open square and a filled-in square are shown, the surface accessibility of that particular residue is not only <20% in the monomer, but its surface accessibility is also decreased by more than a factor of 7 in the dimer. The filled-in and open circles indicate the residues of subunit A that interact with those of subunit B, respectively, and vice versa; the stars indicate the location of the C_2 symmetry axis for each dimer. The designation ht_α indicates a short helical turn. The superposition in (A) was carried out with the program O (*21*) and displayed with the program VISP (*22*). Data for the NMR structure of IL-8 are taken from (*10*).

parallel β sheet, on top of which lie two antiparallel α helices separated by ~14 Å (*10, 11*). In addition, the COOH-terminal end of the helix of each subunit interacts with the underlying sheet of the other subunit (Fig. 3C). In contrast, in the case of hMIP-1β the C_2 axis is located between the CαH protons of Ala^{10} and $Ala^{10'}$; the two helices are 46 Å apart, located on opposite faces of the molecule and oriented approximately orthogonal to each other; strands β1 and β1′ are ~30 Å apart and located on the exterior of the protein; and the dimer interface is formed by the NH_2-terminus (residues 2 to 13), the loop connecting strands β1 and β2 (Leu^{34} and Cys^{35}), and the loop connecting strands β2 and β3 as well as strand β3 (residues 46 to 51) (Figs. 2B and 3, A and B). A comparison of the residues involved in the dimer interfaces of hMIP-1β and IL-8 is provided in Fig. 2B, and a detailed view of the interactions at the dimer interface of hMIP-1β is shown in Fig. 4.

The hMIP-1β dimer is stabilized by both hydrogen bonding and hydrophobic interactions (Fig. 4). There are eight intersubunit backbone hydrogen bonds. Four of the hydrogen bonds make up a small antiparallel β sheet centered around the C_2 axis, which comprises residues 9 to 11 and 9′ to 11′ (strands β0 and β0′). In addition, Asp^6(NH) donates a hydrogen bond to $Gln^{49'}$(O), whereas Asp^6(O) accepts a hydrogen bond from $Cys^{51'}$(NH). In the case of IL-8 there are only six backbone hydrogen bonds between the two subunits (*10, 11*). Despite the extended nature of the hMIP-1β dimer, there is an extensive network of hydrophobic interactions between the two subunits, and eight residues per subunit (the same number as in IL-8) become buried upon dimerization (Fig. 2B). Pro^2, Gly^4, Ser^5, Asp^6, Pro^7, and Pro^8 of the NH_2-terminus of each subunit are in van der Waals contact with residues 46′ to 51′ comprising the turn between strands β2′ and β3′ and strand β3′ of the other subunit. Ser^5 and Asp^6 also interact with $Thr^{16'}$; Pro^7 with $Val^{41'}$ in strand β2′; and Pro^8 with $Ala^{10'}$ and $Cys^{12'}$ in strand β0′, $Tyr^{29'}$ and $Thr^{31'}$ in strand β1′, and $Val^{41'}$ in strand β2′. Finally, Thr^9 interacts with $Phe^{13'}$, and Phe^{13} with

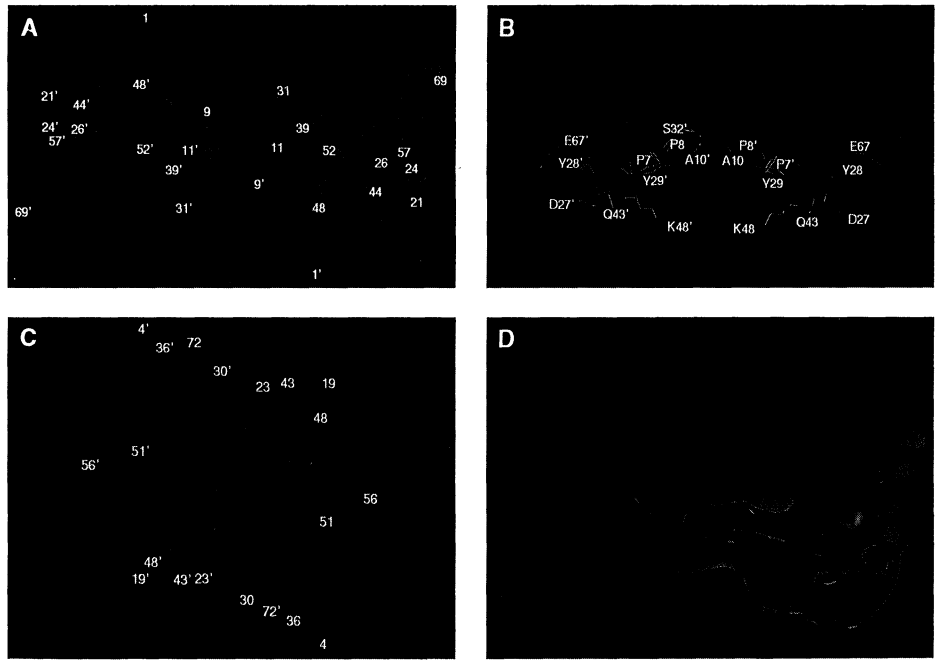

Fig. 3. Schematic ribbon drawings of the hMIP-1β dimer (**A** and **B**), the IL-8 dimer (**C**), and a superposition of the hMIP-1β and IL-8 dimers (**D**) (*20*). In (A), (B), and (C), one subunit is shown in blue and the other in red; in (D), the hMIP-1β subunits are shown in red and orange, whereas the IL-8 subunit is shown in light blue and blue, with the red subunit of hMIP-1β superimposed on the light blue subunit of IL-8 with the same alignment as in Fig. 2. The view of hMIP-1β in (D) is very similar to that in (A). Also shown in (B) are side chains within the cleft of hMIP-1β that may be involved in receptor binding; side chains shown in green are either the same or substituted conservatively in hMIP-1β, hMIP-1α, RANTES, and MCAF (or MCP-1), whereas side chains shown in orange are the same or similar in hMIP-1α and RANTES but different in hMIP-1β or MCAF (or MCP-1). The ribbon diagrams were made with the program RIBBONS (*23*). Data for the NMR structure of IL-8 are taken from (*10*).

Leu$^{34'}$ and Cys$^{35'}$, in the loop connecting strands β1′ and β2′.

Apart from backbone hydrogen bonding, all the interactions that stabilize the dimer in hMIP-1β are hydrophobic in nature, and all but one, consisting of a potential single salt bridge, are hydrophobic in IL-8 (*10, 11*). Dimerization of hMIP-1β monomers to the hMIP-1β– and IL-8–type dimers yields solvation free energy of dimerization (SFED) (*13*) values of −12.5 and −3.3 kcal mol^{-1}, respectively, so that the hMIP-1β–type dimer is favored by −9.2 kcal mol^{-1} over the IL-8–type dimer. In contrast, dimerization of IL-8 monomers to the hMIP-1β– and IL-8–type dimers yields SFED values of −4.6 and −7.0 kcal mol^{-1}, respectively, so that the IL-8–type dimer is favored by −2.4 kcal mol^{-1} over the hMIP-1β–type dimer. These calculations support the proposition that the driving force for the formation and stabilization of the two different types of dimers lies in the burial of hydrophobic residues.

Examination of the structure-based sequence alignment of hMIP-1β and IL-8 (Fig. 2B) yields a possible explanation for this phenomenon. First, IL-8 has an extra four residues at the COOH-terminus that permit extension of the helix onto the adjacent subunit, helping to form the IL-8 dimer. In hMIP-1β, on the other hand, the helix cannot extend beyond the boundaries of its own subunit. Second, in the IL-8 dimer the residues that point upward between the cleft (Leu^{25} and Val^{27}) and across the center of the cleft (Leu^{66}) formed by the two helices are hydrophobic. In contrast, the equivalent three residues in hMIP-1β are polar (Tyr^{28}, Glu^{30}, and Glu^{67}, respectively). The concentration of four partially buried negative charges in very close proximity provided by Glu^{30} and Glu^{67} of each subunit would, on the basis of simple electrostatic considerations, disfavor the formation by hMIP-1β of an IL-8–type dimer. Third, the presence of three proline residues renders the NH_2-terminus of hMIP-1β predominantly hydrophobic, whereas this region is mainly polar in IL-8. Thus, the formation of the hMIP-1β dimer permits burial of these hydrophobic residues.

These differences can be extended to the other α and β chemokines (*2*). In general, the β chemokines have fewer residues at the COOH-terminus than the α chemokines. The sequences NH_2-terminal to the first cysteine residue are always more hydrophobic in the members of the β subfamily than those in the α subfamily. Finally, residues that correspond to Leu^{25}, Val^{27}, and Leu^{66} in IL-8, which are crucial in the stabilization of the IL-8 dimer, are always hydrophobic in the α subfamily and polar in the β subfamily. This suggests that the hMIP-1β and IL-8 dimer structures are most likely preserved in the β and α subfamilies, respectively. In this light, it is likely that the proposed dimeric structure of the β chemokine MCAF (or MCP-1), which we modeled on the basis of the IL-8 dimer, is incorrect (*14*). This only serves to emphasize the importance of direct experimental structure determination, particularly in the case of multimeric systems.

At pH values above 3.5, hMIP-1β aggregates to form small helical fibrils visible in the electron microscope (*15*). These may be of functional relevance with regard to its role in the induction of T cell adhesion (*16*). The pH and salt dependence of this phenomenon suggests an electrostatic basis involving the deprotonation of Asp or Glu residues. An electrostatic potential map of hMIP-1β reveals a clear partitioning of positive and negative charge. In the view shown in Fig. 3B, the latter extends from the bottom right-hand side of the blue subunit to the underside of the molecule, and the former comprises the front surface of the red subunit and the top right-hand side of the blue one. This would easily permit the well-defined association of the positively charged surface of one molecule with the negatively charged surface of another.

The receptors for α and β chemokines fail to show any cross-binding or reactivity between the two subfamilies (*2, 3, 17, 18*). Although the quaternary structure for any receptor-bound chemokine is presently unknown, the different dimeric structures for the α and β chemokines provide an attractive explanation for this observation. We postulate that the large concave surface visible in Fig. 3B, which runs at an angle of approximately 60° to the long axis of the dimer, is involved in receptor binding of the β chemokines. There are two residues on the concave surface of the dimer that are identical in hMIP-1β, MCP-1 (or MCAF), hMIP-1α, and RANTES (Tyr^{28} and Ser^{32}). Furthermore, Pro^{8}, Ala^{10}, Asp^{27}, and Glu^{67} are either the same or substituted conservatively, and we suggest that they play an important role in binding specificity. Of the four β chemokines, only hMIP-1α and RANTES induce a strong calcium flux in the cloned receptor (*17*). This activity may be associated with the four residues (shown in orange in Fig. 3B) in the cleft that are preserved in hMIP-1α and RANTES but are different in hMIP-1β and MCAF (or MCP-1).

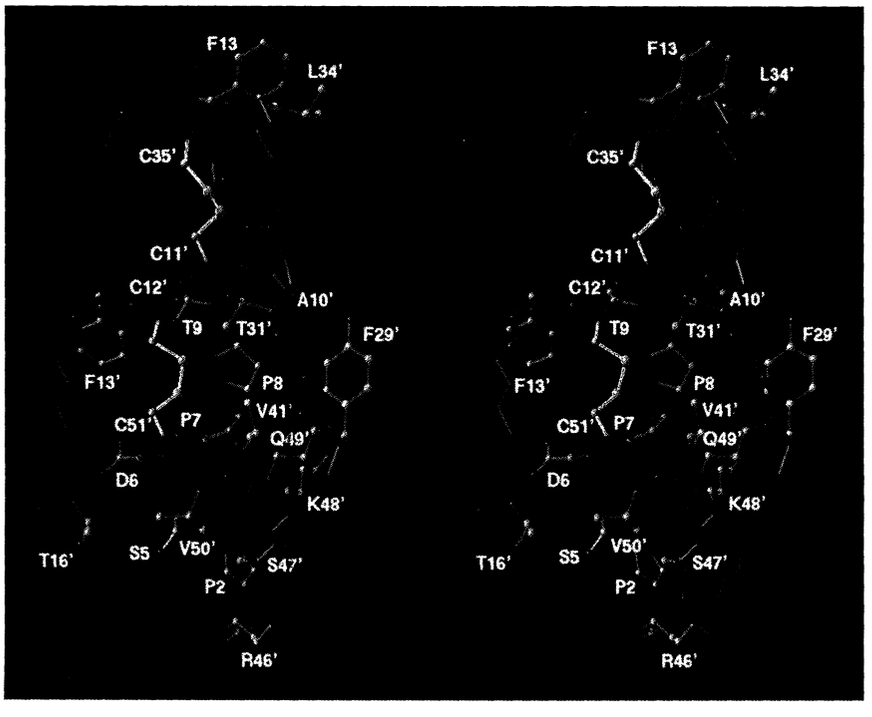

Fig. 4. Stereo view of the dimer interface of hMIP-1β. The backbone and side chains of one subunit are shown in blue and purple, respectively, whereas those of the second subunit are shown in red and green, respectively; the disulfide bridges of the second subunit are shown in yellow. The model was generated with the program VISP (*22*).

REFERENCES AND NOTES

1. M. A. Lipes *et al.*, *Proc. Natl. Acad. Sci. U.S.A.* **85**, 9704 (1988); K. D. Brown *et al.*, *J. Immunol.* **142**, 679 (1989); P. F. Zipfel *et al.*, *ibid.*, p. 1582.
2. J. J. Oppenheim, C. O. C. Zachariae, N. Mukaida, K. Matsushima, *Annu. Rev. Immunol.* **9**, 617 (1991).
3. T. J. Schall, *Cytokine* **3**, 165 (1991); D. T. Taub, K. Conlon, A. R. Lloyd, J. J. Oppenheim, D. J. Kelvin, *Science* **260**, 355 (1993); T. J. Schall *et al.*, *J. Exp. Med.* **177**, 1821 (1993); M. Napolitano, K. B. Seamon, W. J. Leonard, *J. Exp. Med.* **172**, 285 (1990); M. Napolitano *et al.*, *J. Biol. Chem.* **266**, 17531 (1991).
4. Analysis of the analytical ultracentrifugation data indicates that the association constant between monomer and dimer at pH 2.5 is 2.5 × 10^7 M^{-1} (P. T. Wingfield, personal communication). Under the experimental conditions used, the concentration of

monomer present is less than 0.5%. The pH-induced gel formation can be reversed by a high salt concentration (≥1 M NaCl at pH 6), although the sample still exhibits some degree of aggregation at the millimolar concentrations required for NMR studies.

5. Mature hMIP-1β was expressed as a fusion protein with a 30-kD leader sequence in *Escherichia coli*. The recombinant fusion protein, which can constitute up to 50% of the total cell extract, is predominantly found as an insoluble protein in inclusion bodies. The recombinant hMIP-1β fusion protein was solubilized in 7 M guanidine hydrochloride and subjected to a renaturation step [A. van Kimmenade *et al.*, *Eur. J. Biochem.* **173**, 109 (1988)]. The refolded fusion protein was partially purified on a Fast Flow Q (Pharmacia) anion exchange column, and hMIP-1β was cleaved from the fusion partner by treatment with factor Xa. Final purification of hMIP-1β was achieved with a C4 reverse-phase high-performance liquid chromotography column. We achieved uniform (>95%) ^{15}N or ^{13}C labeling by growing the bacteria on minimal medium with $^{15}NH_4Cl$ or [$^{13}C_6$]glucose as the sole sources of N and C, respectively. Samples for NMR contained 1.3 mM isotopically labeled protein subunits (either ^{15}N or both ^{15}N and ^{13}C) in either 100% D_2O or 90% H_2O–10% D_2O (pH 2.5).
6. All NMR experiments were carried out at 35°C on a Bruker AMX600 spectrometer equipped with a *z*-shielded gradient triple resonance probe. We achieved the sequential assignment of the ^1H, ^{13}C, and ^{15}N chemical shifts of hMIP-1β by means of through-bond heteronuclear correlations along the backbone and side chains using the following three-dimensional (3D) experiments: ^{15}N-separated HOHAHA, HNHA, CBCANH, CBCA(CO)NH, HBHA(CO)NH, C(CO)NH, H(CCO)NH, HCCH–correlated spectroscopy (COSY) and HCCH–total correlation spectroscopy to demonstrate CαH(*i*)/CβH(*i*)-$^{15}N(i)$-NH(*i*), CαH(*i*)-$^{15}N(i)$-NH(*i*). ^{13}Cβ/Cα(*i*)-$^{15}N(i)$-NH(*i*) and ^{13}Cβ/Cα(*i* − 1)-$^{15}N(i)$-NH(*i*), ^{13}Cβ/Cα(*i* − 1)-$^{15}N(i)$-NH(*i*), CβH/CαH(*i* − 1)-$^{15}N(i)$-NH(*i*), $^{13}C_j$-(*i* − 1)-$^{15}N(i)$-NH(*i*), $H_j(i-1)$-$^{15}N(i)$-NH(*i*), H_j-$^{13}C_j$-$^{13}C_{j\pm1}$-$H_{j\pm1}$, and H_j-$^{13}C_j$-$^{13}C_{j\pm n}$-$H_{j\pm n}$ correlations, respectively (note that *i* refers to the residue number and *j* to the carbon position along a side chain). Details of these experiments and original references are provided in the following reviews: A. Bax and S. Grzesiek, *Acct. Chem. Res.* **26**, 131 (1993); G. M. Clore and A. M. Gronenborn, *Progr. Nucl. Magn. Reson. Spectrosc.* **23**, 43 (1991); *Methods Enzymol.*, in press; and G. W. Vuister *et al.*, *ibid.* in press. Quantitative $^3J_{HN\alpha}$, $^3J_{CC}$, $^3J_{C\gamma N}$, $^3J_{C\gamma CO}$, and $^3J_{\alpha\beta}$ couplings (where *J* is a coupling constant) were measured from a 3D HNHA spectrum [G. W. Vuister and A. Bax, *J. Am. Chem. Soc.* **115**, 7772 (1993)], a 2D long-range carbon-carbon correlation spectrum [A. Bax, D. Max, D. Zax, *J. Am. Chem. Soc.* **114**, 6923 (1992)], a 2D ^{13}C-{^{15}N} spin-echo difference constant time heteronuclear single quantum coherence spectrum [G. Vuister, A. Wang, A. Bax, *J. Magn. Reson.* **115**, 5334 (1993)], a 2D ^{13}C-{^{13}CO} spin-echo difference constant time heteronuclear single quantum coherence spectrum [S. Grzesiek, G. W. Vuister, A. Bax, *J. Biomol. NMR* **3**, 487 (1993)], and a 2D ^1H-^1H primitive exclusive (PE) COSY spectrum [L. Mueller, *J. Magn. Reson.* **72**, 191 (1987)], respectively. Qualitative $^3J_{\alpha\beta}$, $^3J_{NH\beta}$, and $^3J_{COH\beta}$ couplings were obtained from 3D ^{15}N-separated HOHAHA (*19*), HNHB [S. J. Archer *et al.*, *J. Magn. Reson.* **95**, 636 (1991)], and HN(CO)HB [S. Grzesiek, M. Ikura, G. M. Clore, A. M. Gronenborn, A. Bax, *J. Magn. Reson.* **96**, 215 (1992)] experiments, respectively. Bound water molecules were identified from a 2D ^{15}N-separated rotating frame Overhauser enhancement spectroscopy (ROESY) spectrum recorded with a mixing time of 60 ms with the use of selective excitation of the water resonance together with ^{12}C filtering [S. Grzesiek and A. Bax, *J. Biomol. NMR* **3**, 627 (1993)].
7. The interproton distance restraints were derived from 3D ^{15}N-separated [D. Marion *et al.*, *Biochemistry* **28**, 6150 (1989); E. R. P. Zuiderweg and S. W. Fesik, *ibid.*, p. 2387], 4D ^{15}N/^{13}C-separated [L. E. Kay, G. M. Clore, A. Bax, A. M. Gronenborn, *Science* **249**, 411 (1990)], and 4D ^{13}C/^{13}C-separated [G. M. Clore, L. E. Kay, A. Bax, A. M. Gronenborn, *Biochemistry* **30**, 12 (1991); G. W. Vuister *et al.*, *J. Magn. Reson.* **101**, 210 (1993)] nuclear Overhauser effect (NOE) spectra recorded with mixing times of 120 ms, 120 ms, and 100 ms, respectively. The interproton distance restraints were grouped into three ranges; 1.8 to 2.7 Å (1.8 to 2.9 Å for NOEs involving NH protons), 1.8 to 3.3 Å (1.8 to 3.5 Å for NOEs involving NH protons), and 1.8 to 5.0 Å, corresponding to strong, medium, and weak NOEs, respectively [M. P. Williamson, T. F. Havel, K. Wüthrich, *J. Mol. Biol.* **182**, 295 (1985); G. M. Clore *et al.*, *EMBO J.* **5**, 2729 (1986)]. Upper distance limits for distances involving methyl protons and nonstereospecifically assigned methylene protons were corrected appropriately for center averaging [K. Wüthrich, M. Billeter, W. Braun, *J. Mol. Biol.* **169**, 949 (1983)]. In addition, 0.5 Å was added to the upper limit of distances involving methyl protons to account for the higher apparent intensity of methyl resonances [G. M. Clore, A. M. Gronenborn, M. Nilges, C. A. Ryan, *Biochemistry* **26**, 8012 (1987)]. Stereospecific assignments and φ, ψ, and χ_1 torsion angle restraints were obtained with the conformational grid search program STEREOSEARCH [M. Nilges, G. M. Clore, A. M. Gronenborn, *Biopolymers* **29**, 813 (1990)] on the basis of the $^3J_{HN\alpha}$ and $^3J_{\alpha\beta}$ coupling constants and intraresidue and sequential interresidue interproton distance restraints involving the NH, CαH, and CβH protons derived from 3D ^{15}N- and ^{13}C-separated ROESY experiments (35-ms and 30-ms mixing times, respectively) [G. M. Clore, A. Bax, P. T. Wingfield, A. M. Gronenborn, *Biochemistry* **29**, 5671 (1990)] (*19*). Information from $^3J_{NH\beta}$ and $^3J_{COH\beta}$ coupling constants was also used for identifying the appropriate χ_1 rotamer and for detecting rotamer averaging. Finally, χ_2 torsion angle restraints for Leu residues were obtained from $^3J_{CC}$ coupling constants and the pattern of intraresidue NOEs [R. Powers *et al.*, *Biochemistry* **32**, 6744 (1993)].
8. The structures were calculated with the hybrid distance geometry–simulated annealing protocol [M. Nilges, G. M. Clore, A. M. Gronenborn, *FEBS Lett.* **229**, 317 (1988)], which makes use of the program XPLOR-31 [A. T. Brünger, *XPLOR Version 3.1: A System for X-Ray Crystallography and NMR* (Yale Univ. Press, New Haven, CT, 1993] with minor modifications to ensure symmetry (*10*). The target function that is minimized during simulated annealing comprises only quadratic harmonic potential terms for covalent geometry (that is, bonds, angles, planes, and chirality), square-well quadratic potentials for the experimental distance and torsion angle restraints, a harmonic potential for the $^3J_{HN\alpha}$ coupling constant restraints (J. Kuszewski and G. M. Clore, unpublished results), an effective harmonic potential to maintain symmetry between the two subunits, and a quartic van der Waals repulsion term for the nonbonded contacts. No hydrogen bonding, electrostatic, or 6–12 Lennard-Jones empirical potential energy terms are present in the target function. The final structure calculations were based on 3132 approximate interproton distance restraints (2904 intrasubunit and 228 intersubunit). These were supplemented by 24 restraints for 12 hydrogen bonds involving four tightly bound water molecules, 108 restraints for 54 hydrogen bonds associated with slowly exchanging backbone amide protons, 220 torsion angle restraints (122 φ, 10 ψ, 80 χ_1, and 8 χ_2), 102 $^3J_{HN\alpha}$ coupling constant restraints, and stereospecific assignments for 68 of the 104 β methylene groups and for the methyl groups of 12 of the 14 Val residues and of all 8 Leu residues. (The number of restraints and stereospecific assignments given applies to the dimer; as the dimer is completely symmetric, each observed NOE, for example, gives rise to two interproton distance restraints, one for each subunit.) The coordinates of the 35 final simulated annealing (SA) structures of hMIP-1β, together with the coordinates of the restrained minimized mean structure, (SA)r, and the complete list of experimental NMR restraints and ^1H, ^{15}N, and ^{13}C assignments have been deposited in the Brookhaven Protein Data Bank.
9. Identification of intersubunit NOEs was achieved by two complementary approaches. First, initial structure calculations were carried out on just a single subunit. These indicated the presence of a small but significant number of NOEs that were inconsistent with the structure of the monomer. Thus, for example, NOEs were observed from Asp^6 to Thr^{16}, Val^{50}, and Cys^{51}, and from Phe^{13} to Leu^{34} that have Cα–Cα distances of 28, 24, 22, and 14 Å, respectively, in the monomer. Second, another series of initial calculations based on a dimeric structure was carried out with a simulated annealing strategy in which each calculated interproton distance corresponding to any given NOE restraint was represented by an effective distance given by $0.5[r_{ij}(\text{intra})^{-6} + r_{ij}(\text{inter})^{-6}]^{-1/6}$ (where *r* is distance), thereby allowing the computer to partition the contribution of any given restraint between intra- and intersubunit contributions automatically [M. Nilges, *Proteins Struct. Funct. Genet.* **17**, 297 (1993)]. The starting coordinates for these initial dimer calculations were obtained by manually docking the two monomers on the basis of the NOE restraints, which could be unambiguously assigned to intersubunit interactions in order to generate a very approximate initial model of the dimer. Once the dimer topology was clearly established, an iterative strategy was used to assign all structurally useful intra- and intersubunit NOEs explicitly.
10. G. M. Clore, E. Appella, M. Yamada, K. Matsushima, A. M. Gronenborn, *Biochemistry* **29**, 1689 (1990).
11. E. T. Baldwin *et al.*, *Proc. Natl. Acad. Sci. U.S.A.* **88**, 502 (1991).
12. W. E. Royer Jr., W. E. Love, F. F. Fenderson, *Nature* **316**, 277 (1985); B. Shaanan, H. Lis, N. Sharon, *Science* **254**, 862 (1991).
13. D. Eisenberg and A. D. McLachlan, *Nature* **319**, 199 (1986).
14. A. M. Gronenborn and G. M. Clore, *Protein Eng.* **4**, 263 (1991).
15. A. Stevens, G. M. Clore, A. M. Gronenborn, unpublished observations.
16. Y. Tanaka *et al.*, *Nature* **361**, 79 (1993).
17. K. Neote *et al.*, *Cell* **72**, 415 (1993); J.-L. Gao *et al.*, *J. Exp. Med.* **177**, 1421 (1993).
18. A. K. Samanta *et al.*, *J. Exp. Med.* **169**, 1185 (1989); T. Yoshimura and E. J. Leonard, *J. Immunol.* **145**, 292 (1990); G. J. Graham *et al.*, *Cell Growth Differ.* **4**, 137 (1993); W. E. Holmes, J. Lee, W.-J. Kuang, G. C. Rice, W. I. Wood, *Science* **253**, 1278 (1991); P. M. Murphy and H. L. Tiffany, *ibid.*, p. 1280.
19. G. M. Clore, A. Bax, A. M. Gronenborn, *J. Biomol. NMR* **1**, 13 (1991).
20. Abbreviations for the amino acid residues are: A, Ala; C, Cys; D, Asp; E, Glu; F, Phe; G, Gly; H, His; I, Ile; K, Lys; L, Leu; M, Met; N, Asn; P, Pro; Q, Gln; R, Arg; S, Ser; T, Thr; V, Val; W, Trp; and Y, Tyr.
21. T. A. Jones and M. Kjeldgaard, *O Version 5 Manual* (University of Uppsala, Uppsala, Sweden, 1990).
22. E. de Castro and S. Edelstein, *VISP 1.0 User's Guide* (University of Geneva, Geneva, Switzerland, 1992).
23. M. Carson, *J. Mol. Graphics* **5**, 103 (1987).
24. A. T. Brünger, G. M. Clore, A. M. Gronenborn, R. Saffrich, M. Nilges, *Science* **261**, 328 (1993).
25. B. R. Brooks *et al.*, *J. Comput. Chem.* **74**, 187 (1983).
26. G. M. Clore, M. A. Robien, A. M. Gronenborn, *J. Mol. Biol.* **231**, 82 (1993).
27. We thank A. Bax, D. R. Davies, G. W. Vuister, and S. Grzesiek for useful discussions; F. DeLaglio for the NMR processing package nmrPipe; R. Tschudin and D. Carlson for technical support; P. T. Wingfield for providing the ultracentrifugation data on hMIP-1β; and A. Stevens for examining the hMIP-1β gel under the electron microscope. P.J.L. is a recipient of a Cancer Research Institute–Elisa Heather Halpern postdoctoral fellowship. This work was supported by the AIDS Targeted Antiviral Program of the Office of the Director of NIH (G.M.C., A.M.G., and W.J.L.).

26 October 1993; accepted 2 February 1994